

Formation of Incommensurate Charge Density Waves in Cuprates

H. Miao,^{1,*} R. Fumagalli,² M. Rossi,^{2,3} J. Lorenzana,⁴ G. Seibold,⁵ F. Yakhou-Harris,⁶ K. Kummer,⁶ N. B. Brookes,⁶ G. D. Gu,¹ L. Braicovich,^{2,6} G. Ghiringhelli,^{2,7} and M. P. M. Dean^{1,†}

¹*Condensed Matter Physics and Materials Science Department, Brookhaven National Laboratory, Upton, New York 11973, USA*

²*Dipartimento di Fisica, Politecnico di Milano, Piazza Leonardo da Vinci 32, 20133 Milano, Italy*

³*Stanford Institute for Materials and Energy Sciences, SLAC National Accelerator Laboratory and Stanford University, 2575 Sand Hill Road, Menlo Park, California 94025, USA*

⁴*ISC-CNR, Dipartimento di Fisica, Università di Roma “La Sapienza,” Piazzale Aldo Moro, 00185 Roma, Italy*

⁵*Institut für Physik, BTU Cottbus, P.O. Box 101344, 03013 Cottbus, Germany*

⁶*European Synchrotron Radiation Facility (ESRF), B.P. 220, F-38043 Grenoble Cedex, France*

⁷*CNR/SPIN, Politecnico di Milano, Piazza Leonardo da Vinci 32, 20133 Milano, Italy*

 (Received 22 April 2019; revised manuscript received 5 July 2019; published 6 September 2019)

Although charge density waves (CDWs) are omnipresent in cuprate high-temperature superconductors, they occur at significantly different wave vectors, confounding efforts to understand their formation mechanism. Here, we use resonant inelastic x-ray scattering to investigate the doping- and temperature-dependent CDW evolution in $\text{La}_{2-x}\text{Ba}_x\text{CuO}_4$ ($x = 0.115\text{--}0.155$). We discover that the CDW develops in two stages with decreasing temperature. A precursor CDW with a quasicommensurate wave vector emerges first at high temperature. This doping-independent precursor CDW correlation originates from the CDW phase mode coupled with a phonon and “seeds” the low-temperature CDW with a strongly doping-dependent wave vector. Our observation reveals the precursor CDW and its phase mode as the building blocks of the highly intertwined electronic ground state in the cuprates.

DOI: [10.1103/PhysRevX.9.031042](https://doi.org/10.1103/PhysRevX.9.031042)

Subject Areas: Condensed Matter Physics,
Strongly Correlated Materials,
Superconductivity

A remarkable phenomenon of the cuprates is the coexistence of multiple nearly degenerate electronic orders or instabilities that intertwine at low temperature to form the novel electronic liquid which precipitates high- T_c superconductivity [1,2]. While unidirectional charge density waves (CDWs), also known as stripes, have been theoretically predicted for doped Mott insulators [3–6] and experimentally discovered in La-based cuprates over two decades ago [7], a full CDW phase diagram for different cuprate systems, as shown schematically in Fig. 1(a), was established only very recently [8–18]. Consistent results are also found in state-of-the-art numerical calculations of realistic 2D $t - J$ and Hubbard models near 1/8 doping, where stripe ordering or fluctuations are found to be one of the leading electronic instabilities of the ground state [19–21]. While this progress indicates a universal CDW

mechanism, consensus about the nature of this mechanism has not been reached due to the opposite evolution of the CDW wave vectors with doping in different cuprate families. Figure 1(b) summarizes the doping dependence of the CDW wave vector as determined by diffraction measurements [8,10–12,16,17,22]. In the La-based cuprates, such as $\text{La}_{2-x}\text{Ba}_x\text{CuO}_4$ (LBCO), CDW wave vectors increase with doping and saturate at doping levels beyond $x = 0.125$. In the Bi-, Y-, and Hg-based cuprates, however, CDW wave vectors monotonically decrease with doping. These observations motivate different pictures for CDW formation mechanisms based on either real-space local interactions or weak-coupling Fermi surface (FS) -driven mechanisms [3,4,7,23,24]. However, as is evident from the incommensurate-commensurate crossover in transition-metal chalcogenides [25], low-temperature ordering wave vectors are not necessarily representative of the CDW formation mechanism, which is instead encoded in the inelastic spectrum above the transition temperature. As we show in Fig. 1(c), resonant-inelastic x-ray scattering (RIXS) can probe electronic degrees of freedom via its resonant process [26,27]. Together with the improvement of energy resolution, RIXS can thus reveal CDW order and its fluctuations in great detail.

*hmiao@bnl.gov

†mdean@bnl.gov

Published by the American Physical Society under the terms of the [Creative Commons Attribution 4.0 International license](https://creativecommons.org/licenses/by/4.0/). Further distribution of this work must maintain attribution to the author(s) and the published article's title, journal citation, and DOI.

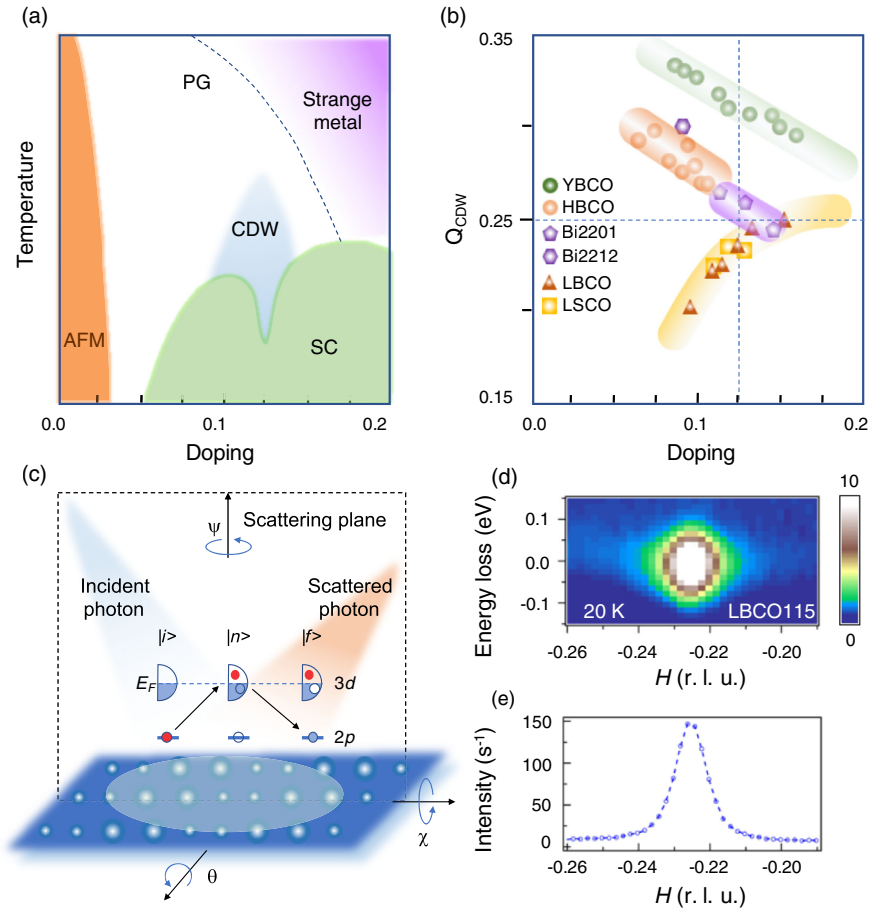


FIG. 1. CDWs in the cuprates. (a) Schematic phase diagram of the cuprates. A ubiquitous CDW dome is observed below the pseudogap temperature and coexists with superconductivity. (b) The doping-dependent CDW wave vector \mathbf{Q}_{CDW} in various cuprate families at low temperature [8,10–12,16,17,22]. (c) schematically shows the L -edge RIXS process and experimental setup. $|i\rangle$, $|n\rangle$, and $|f\rangle$ represent initial, intermediate, and final states, respectively. Solid and empty circles represent occupied and unoccupied states, respectively. (d) Typical RIXS intensity map of $\text{La}_{2-x}\text{Ba}_x\text{CuO}_4$ ($x = 0.115$) at 20 K. The momentum transfer is obtained by rotating the sample about the θ or χ axis. (e) The integrated RIXS intensity in a ± 100 meV energy window of (d) shows a strong CDW peak at $\mathbf{Q}_{\text{CDW}} = 0.225$ r.l.u..

To understand the nature and formation mechanism of the CDW, we use RIXS to study the doping- and temperature-dependent CDW evolution in LBCO_n ($n = 115, 125$, and 155, corresponding to $x = 0.115, 0.125$, and 0.155 in $\text{La}_{2-x}\text{Ba}_x\text{CuO}_4$, respectively). By carefully tracing the doping- and temperature-dependent elastic and inelastic CDW signals in the RIXS spectra, we discover that a doping-independent precursor CDW with a quasicomensurate wave vector first develops at high temperature. This short-ranged CDW correlation originates from the phase mode of the CDW and “seeds” the long-ranged CDW with strong doping-dependent incommensurate wave vectors at a lower temperature. This two-stage CDW evolution uncovers the locally commensurate CDW together with its inelastic excitation as the building block of the charge correlations in the underdoped cuprates and suggests that the doping-dependent incommensurate CDW wave vectors are driven by the subtle balance of intertwined spin, charge, and lattice correlations.

We start by revealing the two-stage CDW evolution in LBCO_{115} . Figures 1(d) and 1(e) show a typical RIXS intensity plot and the integrated RIXS intensity (± 100 meV with respect to zero energy loss) at 20 K. The strong intensity centered at zero energy and $|\mathbf{Q}| = 0.225$ in reciprocal lattice units (r.l.u.) corresponds to static CDW order in LBCO_{115} . RIXS intensity plots of LBCO_{115} below 200 meV at 45 and 35 K are shown in Figs. 2(a) and 2(b), respectively. Representative constant momentum spectra in a wider energy range are shown in Figs. 2(c) and 2(d), where the well-established dispersionless dd excitations (approximately 1.7 eV) and dispersive paramagnon (200–350 meV) are observed [9,16,28,29]. At 45 K, the RIXS spectra below 100 meV are dominated by dispersive charge excitations [identified by red arrows in Figs. 2(a) and 2(c)] whose intensity quickly fades away below $|\mathbf{Q}| \sim 0.2$ r.l.u. This new feature was not observed in previous RIXS studies of this system, due to poorer energy resolution [16,30]. A zero-energy (0 meV) cut of the

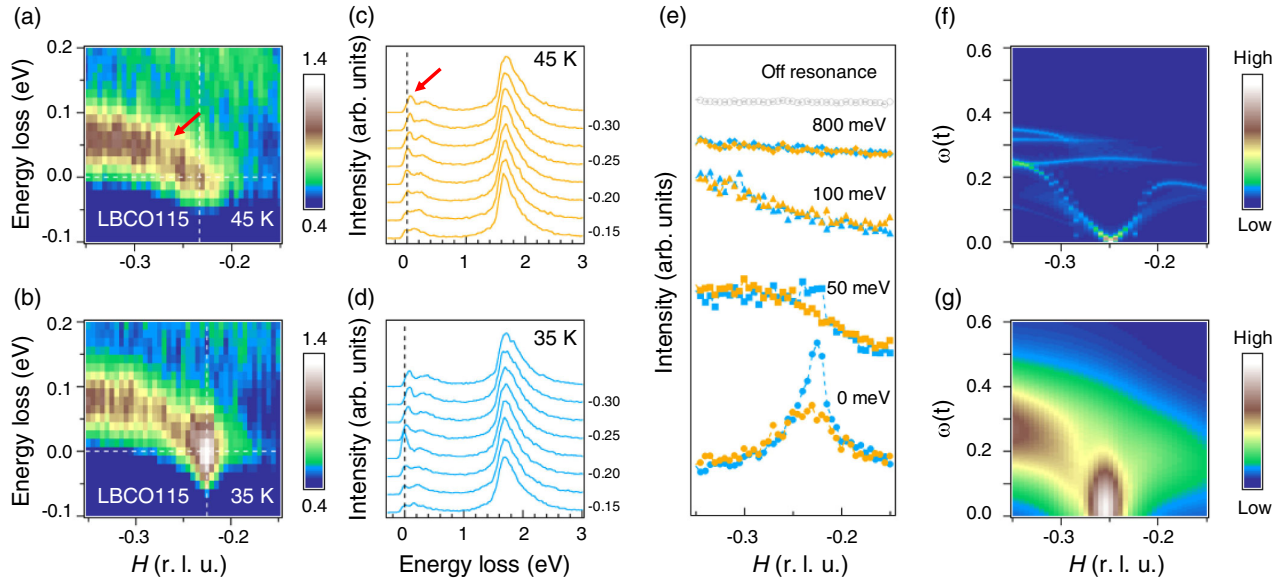


FIG. 2. Two-stage CDW correlations. (a) and (b) show RIXS intensity maps of LBCO115 in a wide momentum transfer range at 45 and 35 K, respectively. Note that the color scales are nearly 10 times smaller than in Fig. 1(d). Representative constant \mathbf{Q} cuts of (a) and (b) are shown in (c) and (d), respectively. Constant E_{loss} cuts of (a) and (b) at $E_{\text{loss}} = 0, 50, 100,$ and 800 meV are shown in (e). The yellow and cyan colors represent data at 45 and 35 K, respectively. Gray squares represent an off-resonant constant E_{loss} cut at 0 meV. Below 500 meV, due to the dispersive charge and paramagnon excitation, the intensity maximum is shifted to larger \mathbf{Q} . At 800 meV, the constant energy cut becomes flat and similar to a nonresonant constant energy cut at zero energy loss. (f) Calculated charge susceptibility along the $(0, 0) \rightarrow (-H, 0)$ direction. The $d = 4$ stripe phase mode couples with the phonon. (g) The same plot as (f) but convoluted with experimental resolution. The energy axes in (f) and (g) are shown in units of $t \approx 0.3$ eV.

intensity plot shows a broad quasielastic peak along the H direction [yellow curve at the bottom in Fig. 2(e)] hereafter referred to as the precursor-CDW peak (PCDW). At a higher energy, the peak position of the constant energy cut shifts to higher \mathbf{Q} , which may affect the \mathbf{Q}_{PCDW} in energy-integrated diffraction studies. This broad peak intensity is completely suppressed when changing the incident photon energy 1.5 eV below the Cu L_3 edge [gray curve in Fig. 2(e)], thus proving that the signal is dominated by the resonant process. The large inelastic contribution and broad peak width of the PCDW suggest dynamic charge fluctuations as discussed extensively in a different cuprate family recently [18]. Intriguingly, Fig. 2(e) shows that H cuts at 50 and 100 meV show a stronger spectral weight at larger values of $|H|$, indicating that dynamic charge correlations may tend to exist at higher $|H|$. It is these higher-energy dynamic correlations that drive the motion of the total energy-integrated CDW peak, and the associated phonon softening, to $H = 0.272$ r.l.u. at higher temperatures of 90 K, although the worse energy resolution of the previous RIXS measurements is insufficient to separate out this effect [16,17]. As we cool down to 35 K, an elastic peak emerges on top of the broad dispersive feature and eventually evolves to the intense CDW peak shown in Fig. 1(d). To distinguish these two CDW peaks, we refer to the low-temperature peak as the low-temperature CDW (LCDW).

To understand the origin of the inelastic excitation and its connection with the CDW, we calculate the dynamic charge

susceptibility $\chi_{\mathbf{q}}^{ee}(\omega)$ of a phenomenological model that reproduces our observations. This calculation assumes the presence of metallic stripes within a correlated Hubbard model at low temperatures; since phonons are known to have large contributions in the energy range of interest [22,31,32], we also include a phonon mode of energy $\Omega_{\mathbf{q}}$, which couples to the electrons with interaction vertex $g_{\mathbf{q}}$. Figures 2(f) and 2(g) show the calculated spectra and the experimental resolution convoluted spectra, respectively. We choose parameters so that the phase mode of the CDW yields an acoustic mode dispersing out from $\mathbf{Q}_{\text{CDW}} = 0.25$ r.l.u. and interacts strongly with the phonon mode at low Q . This regime of soft phasons was invoked before to explain the optical conductivity [33]. Here, the phonon-phason coupling yields the large momentum dependence of the inelastic intensity observed in Figs. 2(a) and 2(b).

Figure 2(g) shows that the model reproduces quite well the features observed at low temperatures even though disorder is neglected. The sensitivity of a CDW to disorder is dictated by its stiffness to local phase changes, i.e., the energy cost to distort the CDW phase locally, so that it can pin to a point defect [25]. A stiff CDW tends to preserve its local phase and will therefore be inefficiently pinned by disorder; whereas a flexible CDW distorts such that it is efficiently pinned. The high-temperature signal is consistent with a flexible PCDW that is strongly pinned by disorder, while the low-temperature features can be assigned to a small fraction of the CDW which becomes

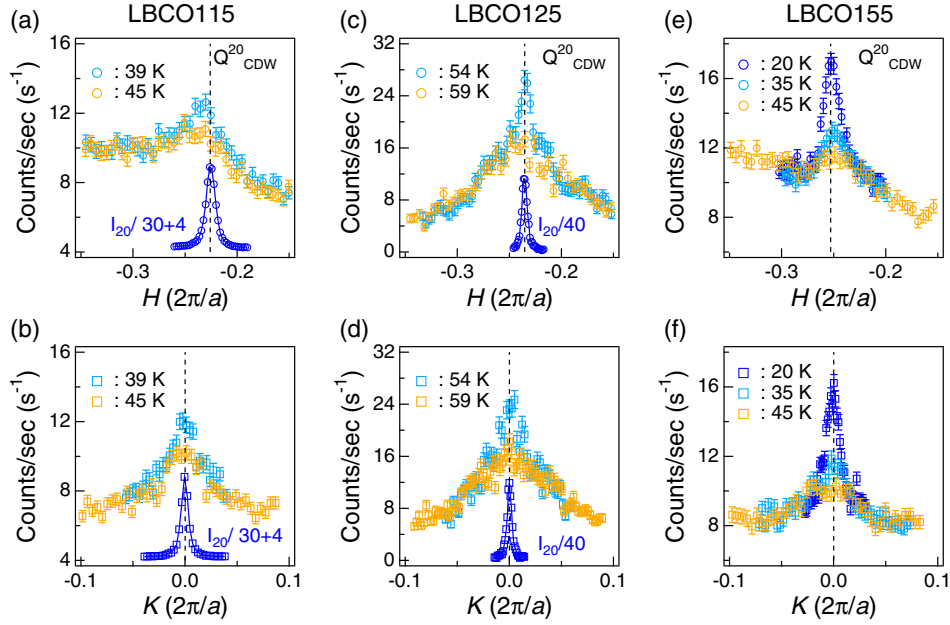


FIG. 3. The doping-dependent evolution of the two-stage CDW. (a) and (b) show the integrated RIXS intensity (± 100 meV with respect to the elastic line) of LBCO115 along the H and K directions, respectively. The same plots of LBCO125 and LBCO155 are shown in (c),(d) and (e),(f), respectively. Blue symbols represent data at 20 K. Because of the large LCDW signal in LBCO115 and LBCO125, the 20 K intensity I_{20} is normalized and offset to $I_{20}/3 + 4$ and $I_{20}/4$ for LBCO115 and LBCO125, respectively. The cyan (yellow) symbols represent the data just below (just above) the critical temperature, where the LCDW starts to emerge. Dashed lines represent \mathbf{Q}_{CDW} at 20 K.

stiff and is therefore inefficiently pinned. This fact can be seen by noting that the total q -integrated scattering from the PCDW is 7 times larger than that from the LCDW [16]. Such a phenomenology explains the concomitant presence of long-range charge order and a well-defined phason mode due to poor pinning. It is worth emphasizing that in the PCDW state the phason mode is still clearly present but yields a broad structure at a low energy.

We now explore the doping-dependent evolution of the two-stage CDW, as enabled by higher RIXS throughput [34]. In Fig. 3, we show the quasielastic RIXS intensity of LBCO115, LBCO125, and LBCO155 along the H and K directions. This intensity is obtained by integrating ± 100 meV with respect to the elastic line in order to achieve a higher sensitivity than cuts at 0 meV. At 20 K (blue symbols), the LCDW peaks are strongly doping dependent. The peak intensity is largest in LBCO125 and significantly weaker in LBCO155, consistent with the LCDW dome being centered at $1/8$ doping [8,11,35]. A similar trend is shown in the correlation length ξ , defined as the inverse peak half width at half maximum ($1/\text{HWHM}$), that is largest in LBCO125 and shortest in LBCO155. The peak position \mathbf{Q}_{LCDW} increases with doping and saturates for $x > 0.125$. Here, x is the hole doping. As we warm up, the intensity of the LCDW decreases and disappears at 41 ± 2 , 55 ± 1 , and 43 ± 3 K in LBCO115, LBCO125, and LBCO155, respectively. Near these critical temperatures, the two-stage CDW structure is evident along both the H and K directions.

To quantify the doping and temperature dependence of the two-stage CDWs, we summarize the fitted CDW peak intensity, HWHM, and the wave vectors in Figs. 4(a) and 4(b) [36]. Most remarkably, as we show in Fig. 4(b), we discovered that, while the wave vectors of the LCDW are strongly doping dependent, the wave vectors of the PCDW are doping independent and broadly peaked at $|\mathbf{Q}_{\text{PCDW}}| = 0.240$ r.l.u. The corresponding real-space CDW period $\lambda_{\text{PCDW}} = 1/\mathbf{Q}_{\text{PCDW}} \sim 16$ Å is similar to the extracted correlation length of PCDW, $\xi_{\text{PCDW}} = 18(2)$, $13(2)$, and $21(3)$ Å for LBCO115, LBCO125, and LBCO155, respectively, and suggests the existence of locally commensurate correlations without extended phase coherence. This picture is also in agreement with our theoretical considerations pointing to a “soft” PCDW that is pinned by disorder. As we go on to discuss, these observations have important implications for the CDW phenomena observed in underdoped cuprates.

Following Fig. 1(b), the wave vector of the CDW appears to fall in two categories with distinct doping-dependent trends. Figure 4(c) illustrates the real-space stripe CDW mechanism, where, by locating holes at the antiphase SDW domain boundaries, the kinetic energy of the strongly correlated electrons is reduced. In this picture, when both the CDW and SDW are static, the CDW wave vector is expected to follow the SDW with a simple $|\mathbf{Q}_{\text{CDW}}| = 2\delta_{\text{SDW}}$ relation that is observed in La-based cuprates at a low temperature and reconfirmed in our RIXS study. When the SDW is dynamic with a spin gap and no magnetic

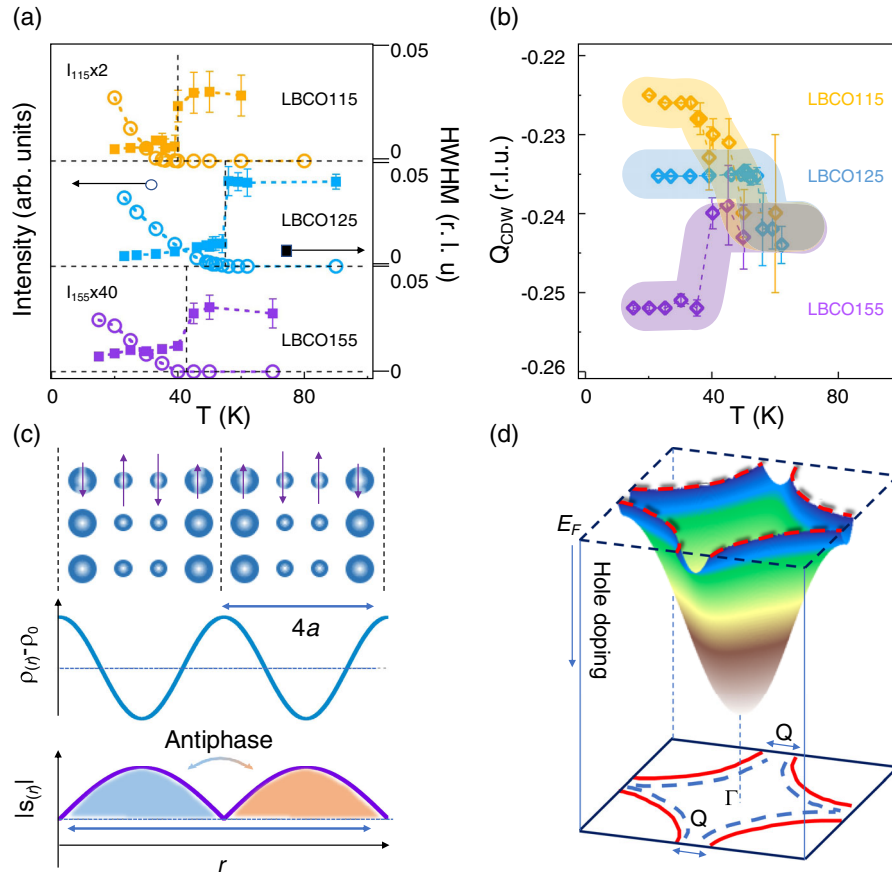


FIG. 4. Universal PCDW. The extracted peak intensity (left axis) and HWHM (right axis) of the PCDW and LCDW are shown in (a). The vertical dashed lines at 38, 55, and 40 K represent the LCDW critical temperature of LBCO115, LBCO125, and LBCO155, respectively. Above these temperatures, both the peak intensity and the HWHM remain unchanged within the error bars. (b) shows the extracted temperature-dependent CDW wave vectors. Note that our measurement is performed at negative Q_{PCDW} to enhance charge excitations [9,16]. The shaded yellow, blue, and purple curves are guides to the eye for LBCO115, LBCO125, and LBCO155, respectively. In the PCDW phase, the wave vectors are doping independent. (c) schematically shows the “stripe” picture from the mean-field theory. Blue circles and purple arrows represent the local hole and spin density, respectively. Antiphase spin density wave (SDW) domains are separated by charge stripes and give rise to the $|Q_{CDW}| = 2\delta_{SDW} \sim 2x$ relation. (d) schematically shows the FS-driven mechanism. Since the FS shrinks at higher hole doping, this model predicts smaller CDW wave vectors at higher doping.

Bragg peak, the CDW wave vector is expected to unlock from the spin correlations with nearly degenerate wave vectors [16,17,20,21,37]. In the FS-based mechanism, the CDW is determined by FS portions with large density of states (DOS), and the free energy is minimized by reducing the DOS near the FS. Since hole doping shifts the chemical potential down in Fig. 4(d), the CDW wave vectors are expected to decrease with doping as is observed in Bi-, Y-, and Hg-based cuprates. Our observations of the PCDW and its phase mode demonstrate that the intrinsic CDW correlations emerge first with doping-independent quasicomensurate periods. This result strongly points towards models in which CDW order is driven by local real-space correlations. Similar short-ranged CDW correlations that persist even to room temperature were recently observed in $YBa_2Cu_3O_{6+\delta}$ (YBCO) [18,38], $Bi_2Sr_2CaCu_2O_{8+\delta}$ (Bi2212) [22], $La_{2-x}Sr_xCuO_4$ (LSCO) [14,39], and

electron-doped $Nd_{2-x}Ce_xCuO_4$ [40], strongly indicating a ubiquitous PCDW phase in underdoped cuprates. Our results are also compatible with previous STM studies of various cuprate families without magnetic stripe order at a low temperature, such as $Bi2212$ and $Ca_{2-x}Na_xCuO_2Cl_2$, where CDWs are found to be locally commensurate with large phase slips [41–43]. The CDW phase mode and the PCDW thus serve as the “seed” of the LCDW that couples strongly to different types of correlations at low temperature and is dragged to distinct wave vectors. An important prerequisite of this picture is that CDW states with different periods are close in free energy. This condition is indeed supported by early computations [44] and recent state-of-the-art numerical studies of a realistic $t - J$ model and a 2D Hubbard model near 1/8 doping [19–21,45], where multiple CDW periods are nearly degenerate in energy. It would be interesting and important for future

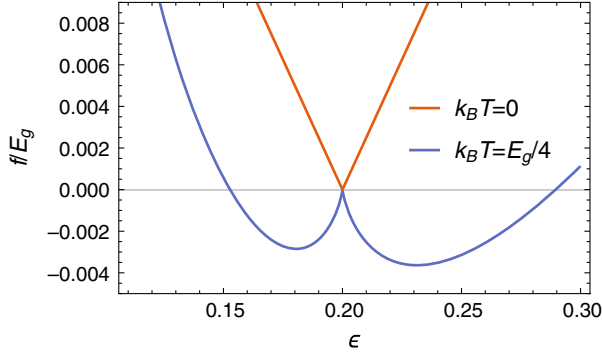


FIG. 5. Free energy per Cu as a function of the incommensurability. Here, we show the free energy of the entropy model at $x = 0.1$ for two different temperatures (in units of the gap due to hole ordering along the charge stripe). At zero temperature the solution with $\epsilon = 2x$ is favored, while at a finite temperature two values of ϵ minimize the energy, with the one having $\epsilon > 2x$ prevailing.

studies to explore the PCDW and its phase mode in heavily underdoped and overdoped cuprates (e.g., LSCO) and build its connections with the puzzling pseudogap and strange metal phase.

Finally, we discuss the temperature-dependent commensurability effect observed in Fig. 4(b). Similar effects are observed in prototypical stripe-ordered $\text{La}_{2-x}\text{Sr}_x\text{NiO}_4$ (LSNO, $x \sim 1/3$). In these materials, the CDW wave vectors also follow a simple $|\mathbf{Q}_{\text{CDW}}| = \delta_{\text{SDW}} \sim x$ relation at low temperature and move to $\mathbf{Q}_{\text{CDW}} = 1/3$ at a high temperature. An entropy-driven self-doping mechanism has been proposed to explain the commensurability effect in LSNO [46]. This model considers the entropy of doped holes as $S = k_B \ln(N_c)$, where N_c is the number of configurations for a given concentration of holes. The number of configurations is computed as the number of ways to accommodate indistinguishable particles in boxes representing equivalent sites along the core of the domain wall that can accommodate holes. We expand the entropy model to our case as described in the Appendix D. This model requires the commonly applied assumption of ordered holes along the stripe so that half filled stripes are insulating with zero entropy and satisfy $|\mathbf{Q}| = 2x$. At finite temperatures, it is convenient to either increase or decrease the incommensurability with respect to the $2x$ value to gain entropy (see Fig. 5). For doping levels below $x = 0.125$, the solution with larger incommensurability has a lower free energy, and the CDW is predicted to be at

$$|\mathbf{Q}| = \frac{\epsilon_0}{1 - e^{-E_g/2k_B T}}, \quad (1)$$

where $\epsilon_0 \sim 2x$ is the low-temperature incommensurability and E_g is the energy gap due to the secondary order along the stripe. For doping levels higher than $x = 0.125$, the computation is more complicated, because stripes overlap

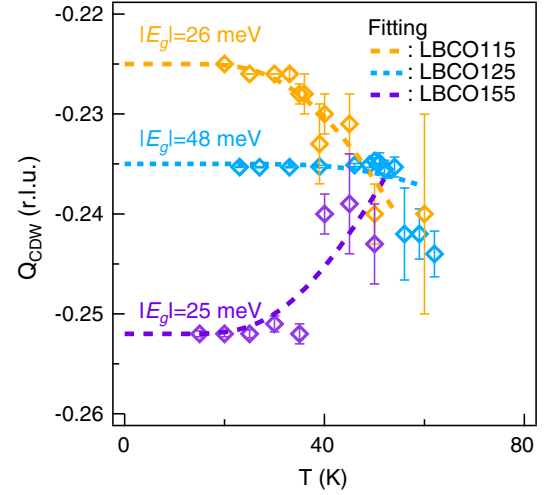


FIG. 6. Entropy-driven self-doping model. The data in Fig. 4(b) are fitted by using Eqs. (1) and (2).

and interstripe interactions become important, producing a saturation of the low-temperature incommensurability [44]. Qualitatively, we expect that the solution in which the incommensurability decreases with temperature prevails, yielding at low temperatures

$$|\mathbf{Q}| = \epsilon_0(1 - e^{-E_g/2k_B T}). \quad (2)$$

This simple computation predicts an activated increase (decrease) of the incommensurability for $x \lesssim 1/8$ ($x \gtrsim 1/8$) as indeed found (see Fig. 6).

In summary, we report detailed measurements of the doping- and temperature-dependent CDW correlations in LBCO. We discover that CDW order forms from a doping-independent PCDW with a quasicommensurate period and a soft phase mode. Our observation thus uncovers the basic foundation underpinning the emergence of CDW order in the cuprates.

ACKNOWLEDGMENTS

H. M. and M. P. M. D. acknowledge V. Bisogni, J. Tranquada, and I. Robinson for insightful discussions. This material is based upon work supported by the U.S. Department of Energy, Office of Basic Energy Sciences, Early Career Award Program under Grant No. 1047478. Work at Brookhaven National Laboratory was supported by the U.S. Department of Energy, Office of Science, Office of Basic Energy Sciences, under Contract No. DE-SC00112704. RIXS measurements were performed at the ID32 beam line of the European Synchrotron Radiation Facility (ESRF). J. L. acknowledges financial support from Italian MAECI through Projects No. SUPERTOP-PGR04879 and No. AR17MO7, from MIUR through Project No. PRIN 2017Z8TS5B, and from Regione Lazio (L. R. 13/08) under project SIMAP.

APPENDIX A: METHODS

$\text{La}_{2-x}\text{Ba}_x\text{CuO}_4$ ($x = 0.115\text{--}0.155$) single crystals were grown using the floating zone method and cleaved *in situ* to reveal a face with a $[001]$ surface normal. The wave vectors used here are described using the high-temperature tetragonal ($I4/mmm$) space group. The orientation matrix is determined by (002) , (101) , and (-101) fundamental peaks at 1700 eV.

RIXS measurements were performed at the ID32 beam line of the European Synchrotron Radiation Facility (ESRF). The resonant condition was achieved by tuning the incident x-ray energy to the maximum of the Cu L_3 absorption peak around 931.5 eV. The scattering geometry is shown in Fig. 1(c). σ and π x-ray polarizations are defined as perpendicular and parallel to the scattering plane, respectively. H and K scans are achieved by rotating the sample around the θ and χ axes, without changing 2θ , thus changing the in-plane component of the momentum transfer $\mathbf{Q} = \mathbf{k}_f - \mathbf{k}_i$. By doing this rotation, we are assuming that the scattering is independent of L , which is reasonable as the interlayer coupling in the cuprates is known to be weak [8,47,48]. All intensities are normalized to the beam current and counting time. In this study, we use σ -polarized incident x rays and negative H values to enhance charge excitations [9,16]. In principle, one can use the polarization analyzer at ID32 to ensure that the excitation is a pure charge mode ($\Delta S = 0$) [40]. However, the efficiency of this setup is an order of magnitude lower than the standard setup, which makes its use very time consuming for the present problem. As a consequence, we cannot completely exclude a spin-flip component of the dispersing mode, although we consider it very unlikely because of the association of the mode with the charge quasielastic scattering. The spectrometer scattering angle (2θ) is fixed at 118° such that $L \approx 1.5$, and the total instrumental energy resolution (full width at half maximum) is set to 55 meV to increase the counting rate. The quasielastic intensity is obtained by integrating the RIXS spectrum in an energy window of ± 100 meV around 0 meV.

APPENDIX B: CHARGE EXCITATIONS OF STRIPES COUPLED TO PHONONS

Our calculations are based on the single-band Hubbard model

$$H = \sum_{i,j,\sigma} t_{ij} c_{i,\sigma}^\dagger c_{j,\sigma} + U \sum_i n_{i,\uparrow} n_{i,\downarrow}, \quad (\text{B1})$$

where we include nearest ($\sim t$) and next-nearest neighbor ($\sim t'$) hopping. Stripe solutions are evaluated within Hartree-Fock (HF), and we calculate binding energies with respect to the homogeneous antiferromagnet (AFM) for a configuration where the domain wall of the AFM order parameter is bond centered. Within the HF approximation,

site-centered stripes involve paramagnetic sites with charge density n , and the associated energy cost $\sim Un^2/4$ makes them energetically unfavorable with respect to bond-centered configurations for large U . This is not anymore the case if correlations beyond the HF approximation are taken into account [49]. Here, for simplicity, we keep the HF approximation but choose parameters $U/t = 4$ and $t'/t = -0.25$ which reproduce the ‘‘Yamada plot’’ [50], i.e., the low-temperature relation between spin incommensurability δ_{SDW} and doping, $x = \delta_{\text{SDW}}$ [see Fig. 4(c)].

Excitations on top of the mean-field stripes are computed with the random phase approximation (RPA). The striped ground state couples charge fluctuations $\delta\rho_{\mathbf{q}}$ which differ by multiples α of the stripe modulation wave vector \mathbf{Q}_s with α an integer. Moreover, charge fluctuations are coupled with fluctuations of the magnetization $\delta m_{\mathbf{q}+\alpha\mathbf{Q}_s}$ so that for each α, β the susceptibility is a 2×2 matrix:

$$\underline{\underline{\chi}}_{\alpha,\beta}(\mathbf{q}) = \begin{pmatrix} \chi_{\alpha,\beta}^{\rho,\rho}(\mathbf{q}) & \chi_{\alpha,\beta}^{\rho,m}(\mathbf{q}) \\ \chi_{\alpha,\beta}^{m,\rho}(\mathbf{q}) & \chi_{\alpha,\beta}^{m,m}(\mathbf{q}) \end{pmatrix}.$$

The total susceptibility matrix is then of dimension $2\lambda_{\text{mag}} \times 2\lambda_{\text{mag}}$, where λ_{mag} is the magnetic periodicity (in units of the lattice spacing). The corresponding RPA equation reads

$$\underline{\underline{\chi}}^{ee}(\mathbf{q}) = \underline{\underline{\chi}}^0(\mathbf{q}) + \underline{\underline{\chi}}^0(\mathbf{q}) \underline{\underline{V}}^{ee}(\mathbf{q}) \underline{\underline{\chi}}(\mathbf{q}) \quad (\text{B2})$$

with the interaction given by

$$\underline{\underline{V}}_{\alpha,\beta}(\mathbf{q}) = \begin{pmatrix} \frac{U}{2} & 0 \\ 0 & -\frac{U}{2} \end{pmatrix} \delta_{\alpha,\beta}.$$

Upon including also the coupling to lattice fluctuations (vertex $g_{\mathbf{q}}$ and frequency $\Omega_{\mathbf{q}}$), the renormalized phonon propagator can be obtained from

$$\underline{\underline{D}}(\mathbf{q}, \omega) = [\underline{\underline{1}} + \underline{\underline{\Lambda}}(\mathbf{q}) \underline{\underline{D}}^0(\mathbf{q}, \omega) \underline{\underline{\chi}}_{ee}(q, \omega) \underline{\underline{\Lambda}}(\mathbf{q})]^{-1} \underline{\underline{D}}^0(\mathbf{q}, \omega),$$

where $\underline{\underline{\chi}}_{ee}(\mathbf{q}, \omega)$ is evaluated from Eq. (B2). The vertex and phonon Green’s function matrices are given, respectively, by

$$\underline{\underline{\Lambda}}_{\alpha,\beta}(\mathbf{q}) = \begin{pmatrix} g_{\mathbf{q}+\mathbf{Q}_\alpha} & 0 \\ 0 & 0 \end{pmatrix} \delta_{\alpha,\beta},$$

$$\underline{\underline{D}}_{\alpha,\beta}^0(\mathbf{q}) = \begin{pmatrix} D_0(\mathbf{q} + \mathbf{Q}_\alpha, \omega) & 0 \\ 0 & 0 \end{pmatrix} \delta_{\alpha,\beta}$$

with the bare phonon Green’s function

$$D_0(\mathbf{q}, \omega) = \frac{2\Omega_{\mathbf{q}}}{\omega^2 - \Omega_{\mathbf{q}}^2}.$$

The phonon propagator can then be used to compute the phonon contribution to RIXS following the approach in Ref. [31].

In the main part of the paper, we show results for a longitudinal acoustic phonon with frequency and coupling given, respectively, by

$$\begin{aligned}\Omega_{\mathbf{q}} &= \Omega_0 \sqrt{\sin^2 \frac{\mathbf{q}_x}{2} + \sin^2 \frac{\mathbf{q}_y}{2}}, \\ g_{\mathbf{q}} &= g_0 \sqrt{\sin^2 \frac{\mathbf{q}_x}{2} + \sin^2 \frac{\mathbf{q}_y}{2}}.\end{aligned}$$

The stripe phason mixes phonons which differ by a reciprocal lattice vector of the stripe lattice. This coupling is particularly strong at the stripe momentum $\mathbf{Q}_{\text{CDW}} = (0.25, 0)$, where it can induce a quasicritical mode due to a change of the respective stability of bond- and site-centered stripes similar to Ref. [33]. This mode is shown in Figs. 1(g) and 1(f) for $\Omega_0/t = 0.42$ and $g_0/t = 0.73$, respectively.

We shall note that (i) Ω_0 is the “bare” phonon energy, which is renormalized by the electron-phonon coupling to an energy of the order of 70–80 meV for $t \sim 0.3$ eV; (ii) the optical phonon is also active in the energy range of interest, and in this case the prominent asymmetric intensity distribution [Figs. 2(a) and 2(b)] is possibly caused by the more complicated cross-section effect of the RIXS process [26], which we do not take into account in our model calculations.

APPENDIX C: COMMENSURATE VS INCOMMENSURATE CDW

A commensurate CDW with period Ma_0 is known to have a strong lattice effect. Charge modulations mix electronic states with momentum $k + nQ_{\text{CDW}}$ (n is an integer) and yield an additional phase-dependent condensation energy [51]. As the temperature changes, this additional commensurate energy may thus drive an incommensurate to commensurate crossover. In mean-field theory for a 1D CDW, the approximate crossover condition for $M = 4$ is formulated as

$$\left| 4a_0 - \frac{1}{Q_{\text{CDW}}} \right| \leq \frac{2\pi^2 E_{\text{cond}}}{\lambda_{\text{epc}}^{1/2} D}, \quad (\text{C1})$$

where $E_{\text{cond}} = \frac{1}{2}n(\epsilon_F)\Delta_{\text{CDW}}^2$ is the phase-independent CDW condensation energy, Δ_{CDW} is the CDW gap, D is the cutoff energy close to the bandwidth or Fermi energy, and λ_{epc} is a dimensionless electron-phonon coupling constant [25]. Evidence for this effect has been observed in conventional CDW materials, such as $\text{K}_{0.3}\text{MoO}_4$, TaS_3 , and NdSe_3 [25], where the CDW wave vector is temperature dependent and

becomes commensurate at the base temperature. This CDW evolution differs from our observations, where the commensurate CDW forms at a high temperature and persists to a low temperature.

It is worth noting that the PCDW is short ranged without long-range phase coherence. Since the multiple CDW periods are nearly degenerate in energy [19–21], it is reasonable to expect that multiple CDW periods coexist with $\lambda = 4a_0$ being statistically dominated. This situation might be the reason why \mathbf{Q}_{PCDW} is slightly off 0.25 r.l.u. If possible, it would be interesting to directly check this expectation in a future STM study.

APPENDIX D: ENTROPY MODEL FOR CUPRATE STRIPES

Ishizaka *et al.* [46] consider a successful model to explain the shift of incommensurability with temperature in nickelates. Here, we first briefly review their model. They consider the entropy of doped holes as $S = k_B \ln(N_c)$, where N_c is the number of configurations for a given concentration of holes. The number of configurations is computed as the number of ways to accommodate indistinguishable particles in boxes representing equivalent sites along the core of the domain wall that can accommodate holes. Nickelates have insulating stripes at $T = 0$. For filled stripes, there is only one configuration ($N_c = 1$) and $S = 0$. If the distance between the stripes is decreased at fixed x , there are not enough holes to fill completely all stripe core sites. Calling δ the concentration of electrons, the incommensurability ϵ is now determined by the total number of domain wall sites or boxes being occupied by holes (concentration x) or electrons (concentration δ), namely, $\epsilon = x + \delta$. If there are N total Ni sites in the system, the entropy is

$$\begin{aligned}S &= k_B \ln \frac{N_{\text{box}}!}{N_{\text{el}}!(N_{\text{box}} - N_{\text{el}})!} \\ &= k_B N [\epsilon \ln \epsilon - \delta \ln \delta - (\epsilon - \delta) \ln(\epsilon - \delta)].\end{aligned} \quad (\text{D1})$$

Here, we use the relation $\ln N! = N \ln N - N$ for $N \rightarrow \infty$. The computation is completed by postulating that the total energy is $E = \mu^- \delta N$, where μ^- is the energy to remove holes. Notice that this expression holds only for $\delta > 0$. For hole addition, a different energy is involved, because the stripes are filled and the AFM regions have to accommodate the holes. We call that energy μ^+ . The fact that μ^- and μ^+ are different means simply that the filled stripe is an insulator and there is a jump in the chemical potential around $\delta = 0$. To generalize this model to cuprates, one should first identify the particles and the boxes, which is less trivial than in nickelates. For vertical stripes as in cuprates, if d is the distance among domains (in units of the lattice constant a), the charge incommensurability is $\epsilon = 1/d$. The first model of stripes [3] assumes insulating

stripes as in nickelates, and this assumption leads to $\epsilon = x$. However, in the cuprates, $\epsilon = 2x$ is observed for $x < 1/8$ [7,8], which leads to half filled stripes. From the theory side, a more accurate computation [44] indeed predicts half filled stripes in accord with the experiment. On the other hand, metallic half filled stripes pose a problem for the entropy model, since the half filled system has maximum entropy. Therefore, the temperature will only stabilize this configuration more, and the incommensurability would be independent of the temperature in contradiction with the experiment. However, as we show in Fig. 1(a), the CDW is enhanced around $x = 1/8$. It is proposed by White and Scalapino [52] that this 1/8 anomaly is due to the tendency of stripes to develop additional hole ordering along the stripe [44]. Indeed, assuming stripes in neighboring planes are perpendicular to each other, the Coulomb potential of one plane favors a half filled CDW along the stripe in the next plane only at $x = 1/8$, consistent with the increased stability of the CDW at that doping.

We can assume that decreasing the doping in this configuration is still favorable as suggested by mean-field computations which picture the secondary CDW along the stripe as a lattice of Copper pair singlets [53]. In strong coupling, the pattern along the stripe is $00\uparrow\downarrow 00\uparrow\downarrow$, where 00 and $\uparrow\downarrow$ represent holes and disordered spins, respectively. Notice that this pattern has different periodicity than the pattern often assumed, $\uparrow 0\uparrow 0\downarrow$. Since at $T = 0$ this state would be nominally insulating, we assume again that the energy to add or remove hole is different; i.e., the pattern of site diagonal energy is assumed to be $\mu^- \mu^- \mu^+ \mu^+ \mu^- \mu^- \mu^+ \mu^+$. As for the nickelates, this configuration has zero entropy. We now compute the entropy associated with an increase of the incommensurability, i.e., a decrease of d at fixed x . The incommensurability in this case satisfies $x + \delta = \epsilon/2$, where δ is the concentration of extra electrons. The entropy reads

$$S = k_B N \left[\frac{\epsilon}{2} \ln \frac{\epsilon}{2} - |\delta| \ln |\delta| - \left(\frac{\epsilon}{2} - |\delta| \right) \ln \left(\frac{\epsilon}{2} - |\delta| \right) \right], \quad (\text{D2})$$

where N is the number of Cu sites and for simplicity we neglect the entropy due to the spin degrees of freedom, which does not change the physics.

If we consider a decrease of the incommensurability, $x + \delta = \epsilon/2$ is still valid if we allow δ to be negative and interpret $-\delta$ as the concentration of holes added to μ^+ sites. For fixed ϵ , the entropy of the ordered half filled stripe is symmetric with respect to adding or removing holes, so Eq. (D2) holds as written with the modulus, and the energy can be written as $e = |\delta| E_g/2$, where we take $\mu^\pm = \pm E_g/2$ so the free energy is also symmetric. Notice, however, that the latter has to be minimized with respect to ϵ at fixed x , which is not anymore symmetric. Indeed, there are two solutions which minimize the free energy at finite temperature as shown in Fig. 5, having either $\epsilon < 2x$ or $\epsilon > 2x$ and

deviating from the zero temperature solution $\epsilon = 2x$. The solution in which the incommensurability increases with temperature has a lower free energy and leads to Eq. (1). For $x > 1/8$, the interaction between domain walls has to be taken into account [44]. A detailed theoretical study is left for future work, as it goes beyond our present scope. In particular, it would require adding additional terms to the energy that makes the low-temperature incommensurability saturate at $\epsilon \sim 1/4$ and include the effect of Fermi surface wrapping, which frustrates the secondary order along the stripe [54]. For simplicity, here we neglect these effects and simply assume the solution in which the incommensurability decrease with the temperature is favored due to the lower energetic cost. This assumption leads to Eq. (2) for doping larger than 1/8.

We note that our entropy model can qualitatively explain the incommensurate-commensurate crossover below or near the LCDW transition temperature; it, however, does not yield the saturation of ϵ_0 as a function of doping or temperature due to the crude approximations. Figure 6 shows a fit of experimental data below 60 K by using Eqs. (1) and (2). We also note that experimental studies of YBCO suggest that the local commensurate period is more consistent with $3a_0$ [38], which might be due to the special chain structure that favors a different period. A more sophisticated model incorporating the unidirectional field may be needed to explain the result in YBCO.

-
- [1] E. Fradkin, S. A. Kivelson, and J. M. Tranquada, *Colloquium: Theory of Intertwined Orders in High Temperature Superconductors*, *Rev. Mod. Phys.* **87**, 457 (2015).
 - [2] P. A. Lee, *Amperean Pairing and the Pseudogap Phase of Cuprate Superconductors*, *Phys. Rev. X* **4**, 031017 (2014).
 - [3] J. Zaanen and O. Gunnarsson, *Charged Magnetic Domain Lines and the Magnetism of High- T_c Oxides*, *Phys. Rev. B* **40**, 7391 (1989).
 - [4] D. Poilblanc and T. M. Rice, *Charged Solitons in the Hartree-Fock Approximation to the Large- U Hubbard Model*, *Phys. Rev. B* **39**, 9749 (1989).
 - [5] V. J. Emery, S. A. Kivelson, and H. Q. Lin, *Phase Separation in the t - J Model*, *Phys. Rev. Lett.* **64**, 475 (1990).
 - [6] C. Castellani, C. Di Castro, and M. Grilli, *Singular Quasiparticle Scattering in the Proximity of Charge Instabilities*, *Phys. Rev. Lett.* **75**, 4650 (1995).
 - [7] J. M. Tranquada, B. J. Sternlieb, J. D. Axe, Y. Nakamura, and S. Uchida, *Evidence for Stripe Correlations of Spins and Holes in Copper Oxide Superconductors*, *Nature (London)* **375**, 561 (1995).
 - [8] M. Hücker, M. v. Zimmermann, G. D. Gu, Z. J. Xu, J. S. Wen, G. Xu, H. J. Kang, A. Zheludev, and J. M. Tranquada, *Stripe Order in Superconducting $\text{La}_{2-x}\text{Ba}_x\text{CuO}_4$ ($0.095 \leq x \leq 0.155$)*, *Phys. Rev. B* **83**, 104506 (2011).
 - [9] G. Ghiringhelli *et al.*, *Long-Range Incommensurate Charge Fluctuations in $(Y, \text{Nd})\text{Ba}_2\text{Cu}_3\text{O}_{6+x}$* , *Science* **337**, 821 (2012).

- [10] S. Blanco-Canosa, A. Frano, E. Schierle, J. Porras, T. Loew, M. Minola, M. Bluschke, E. Weschke, B. Keimer, and M. Le Tacon, *Resonant X-Ray Scattering Study of Charge-Density Wave Correlations in $\text{YBa}_2\text{Cu}_3\text{O}_{6+x}$* , *Phys. Rev. B* **90**, 054513 (2014).
- [11] W. Tabis *et al.*, *Synchrotron X-Ray Scattering Study of Charge-Density-Wave Order in $\text{HgBa}_2\text{CuO}_{4+\delta}$* , *Phys. Rev. B* **96**, 134510 (2017).
- [12] R. Comin, A. Frano, M. M. Yee, Y. Yoshida, H. Eisaki, E. Schierle, E. Weschke, R. Sutarto, F. He, A. Soumyanarayanan, Y. He, M. Le Tacon, I. S. Elfimov, J. E. Hoffman, G. A. Sawatzky, B. Keimer, and A. Damascelli, *Charge Order Driven by Fermi-Arc Instability in $\text{Bi}_2\text{Sr}_{2-x}\text{La}_x\text{CuO}_{6+\delta}$* , *Science* **343**, 390 (2014).
- [13] P. Abbamonte, A. Rusydi, S. Smadici, G. D. Gu, G. A. Sawatzky, and D. L. Feng, *Spatially Modulated “Mottness” in $\text{La}_{2-x}\text{Ba}_x\text{CuO}_4$* , *Nat. Phys.* **1**, 155 (2005).
- [14] T. P. Croft, C. Lester, M. S. Senn, A. Bombardi, and S. M. Hayden, *Charge Density Wave Fluctuations in $\text{La}_{2-x}\text{Sr}_x\text{CuO}_4$ and Their Competition with Superconductivity*, *Phys. Rev. B* **89**, 224513 (2014).
- [15] V. Thampy, M. P. M. Dean, N. B. Christensen, L. Steinke, Z. Islam, M. Oda, M. Ido, N. Momono, S. B. Wilkins, and J. P. Hill, *Rotated Stripe Order and Its Competition with Superconductivity in $\text{La}_{1.88}\text{Sr}_{0.12}\text{CuO}_4$* , *Phys. Rev. B* **90**, 100510 (R) (2014).
- [16] H. Miao, J. Lorenzana, G. Seibold, Y. Y. Peng, A. Amorese, F. Yakhov-Harris, K. Kummer, N. B. Brookes, R. M. Konik, V. Thampy, G. D. Gu, G. Ghiringhelli, L. Braicovich, and M. P. M. Dean, *High-Temperature Charge Density Wave Correlations in $\text{La}_{1.875}\text{Ba}_{0.125}\text{CuO}_4$ without Spin-Charge Locking*, *Proc. Natl. Acad. Sci. U.S.A.* **114**, 12430 (2017).
- [17] H. Miao, D. Ishikawa, R. Heid, M. Le Tacon, G. Fabbris, D. Meyers, G. D. Gu, A. Q. R. Baron, and M. P. M. Dean, *Incommensurate Phonon Anomaly and the Nature of Charge Density Waves in Cuprates*, *Phys. Rev. X* **8**, 011008 (2018).
- [18] R. Arpaia, S. Caprara, R. Fumagalli, G. De Vecchi, Y. Y. Peng, E. Anderson, D. Betto, G. M. De Luca, N. B. Brookes, F. Lombardi, M. Salluzzo, L. Braicovich, C. Di Castro, M. Grilli, and G. Ghiringhelli, *Dynamical Charge Density Fluctuations Pervading the Phase Diagram of a Cu-Based High- T_c Superconductor*, [arXiv:1809.04949](https://arxiv.org/abs/1809.04949).
- [19] P. Corboz, T. M. Rice, and M. Troyer, *Competing States in the t - J Model: Uniform d -Wave State versus Stripe State*, *Phys. Rev. Lett.* **113**, 046402 (2014).
- [20] E. W. Huang, C. B. Mendl, S. Liu, S. Johnston, H.-C. Jiang, B. Moritz, and T. P. Devereaux, *Numerical Evidence of Fluctuating Stripes in the Normal State of High- T_c Cuprate Superconductors*, *Science* **358**, 1161 (2017).
- [21] B.-X. Zheng, C.-M. Chung, P. Corboz, G. Ehlers, M.-P. Qin, R. M. Noack, H. Shi, S. R. White, S. Zhang, and G. K.-L. Chan, *Stripe Order in the Underdoped Region of the Two-Dimensional Hubbard Model*, *Science* **358**, 1155 (2017).
- [22] L. Chaix, G. Ghiringhelli, Y. Y. Peng, M. Hashimoto, B. Moritz, K. Kummer, N. B. Brookes, Y. He, S. Chen, S. Ishida, Y. Yoshida, H. Eisaki, M. Salluzzo, L. Braicovich, Z.-X. Shen, T. P. Devereaux, and W.-S. Lee, *Dispersive Charge Density Wave Excitations in $\text{Bi}_2\text{Sr}_2\text{CaCu}_2\text{O}_{8+\delta}$* , *Nat. Phys.* **13**, 952 (2017).
- [23] R. Comin, R. Sutarto, E. H. da Silva Neto, L. Chauviere, R. Liang, W. N. Hardy, D. A. Bonn, F. He, G. A. Sawatzky, and A. Damascelli, *Broken Translational and Rotational Symmetry via Charge Stripe Order in Underdoped $\text{YBa}_2\text{Cu}_3\text{O}_{6+y}$* , *Science* **347**, 1335 (2015).
- [24] K. M. Shen, F. Ronning, D. H. Lu, F. Baumberger, N. J. C. Ingle, W. S. Lee, W. Meevasana, Y. Kohsaka, M. Azuma, M. Takano, H. Takagi, and Z.-X. Shen, *Nodal Quasiparticles and Antinodal Charge Ordering in $\text{Ca}_{2-x}\text{Na}_x\text{CuO}_2\text{Cl}_2$* , *Science* **307**, 901 (2005).
- [25] G. Grüner, *Density Waves in Solids* (CRC Press, Boca Raton, 2018), pp. 1–288.
- [26] L. J. P. Ament, M. van Veenendaal, T. P. Devereaux, J. P. Hill, and J. van den Brink, *Resonant Inelastic X-Ray Scattering Studies of Elementary Excitations*, *Rev. Mod. Phys.* **83**, 705 (2011).
- [27] M. P. M. Dean, *Insights into the High Temperature Superconducting Cuprates from Resonant Inelastic X-Ray Scattering*, *J. Magn. Magn. Mater.* **376**, 3 (2015).
- [28] M. P. M. Dean, R. S. Springell, C. Monney, K. J. Zhou, J. Pereiro, I. Božović, B. Dalla Piazza, H. M. Rønnow, E. Morenzoni, J. van den Brink, T. Schmitt, and J. P. Hill, *Spin Excitations in a Single La_2CuO_4 Layer*, *Nat. Mater.* **11**, 850 (2012).
- [29] M. Le Tacon, G. Ghiringhelli, J. Chaloupka, M. M. Sala, V. Hinkov, M. W. Haverkort, M. Minola, M. Bakr, K. J. Zhou, S. Blanco-Canosa, C. Monney, Y. T. Song, G. L. Sun, C. T. Lin, G. M. De Luca, M. Salluzzo, G. Khaliullin, T. Schmitt, L. Braicovich, and B. Keimer, *Intense Paramagnon Excitations in a Large Family of High-Temperature Superconductors*, *Nat. Phys.* **7**, 725 (2011).
- [30] M. P. M. Dean, G. Dellea, M. Minola, S. B. Wilkins, R. M. Konik, G. D. Gu, M. Le Tacon, N. B. Brookes, F. Yakhov-Harris, K. Kummer, J. P. Hill, L. Braicovich, and G. Ghiringhelli, *Magnetic Excitations in Stripe-Ordered $\text{La}_{1.875}\text{Ba}_{0.125}\text{CuO}_4$ Studied Using Resonant Inelastic X-Ray Scattering*, *Phys. Rev. B* **88**, 020403(R) (2013).
- [31] T. P. Devereaux, A. M. Shvaika, K. Wu, K. Wohlfeld, C. J. Jia, Y. Wang, B. Moritz, L. Chaix, W.-S. Lee, Z.-X. Shen, G. Ghiringhelli, and L. Braicovich, *Directly Characterizing the Relative Strength and Momentum Dependence of Electron-Phonon Coupling Using Resonant Inelastic X-Ray Scattering*, *Phys. Rev. X* **6**, 041019 (2016).
- [32] D. Reznik, L. Pintschovius, M. Ito, S. Iikubo, M. Sato, H. Goka, M. Fujita, K. Yamada, G. D. Gu, and J. M. Tranquada, *Electron-Phonon Coupling Reflecting Dynamic Charge Inhomogeneity in Copper Oxide Superconductors*, *Nature (London)* **440**, 1170 (2006).
- [33] J. Lorenzana and G. Seibold, *Dynamics of Metallic Stripes in Cuprates*, *Phys. Rev. Lett.* **90**, 066404 (2003).
- [34] N. B. Brookes, F. Yakhov-Harris, K. Kummer, A. Fondacaro, J. C. Cezar, D. Betto, E. Velez-Fort, A. Amorese, G. Ghiringhelli, L. Braicovich, R. Barrett, G. Berruyer, F. Cianciosi, L. Eybert, P. Marion, P. van der Linden, and L. Zhang, *The Beamline Id32 at the ESRF for Soft X-Ray High Energy Resolution Resonant Inelastic X-Ray Scattering and Polarisation Dependent X-Ray Absorption Spectroscopy*, *Nucl. Instrum. Methods Phys. Res., Sect. A* **903**, 175 (2018).

- [35] S. Blanco-Canosa, A. Frano, T. Loew, Y. Lu, J. Porras, G. Ghiringhelli, M. Minola, C. Mazzoli, L. Braicovich, E. Schierle, E. Weschke, M. Le Tacon, and B. Keimer, *Momentum-Dependent Charge Correlations in $\text{YBa}_2\text{Cu}_3\text{O}_{6+\delta}$ Superconductors Probed by Resonant X-Ray Scattering: Evidence for Three Competing Phases*, *Phys. Rev. Lett.* **110**, 187001 (2013).
- [36] See Supplemental Material at <http://link.aps.org/supplemental/10.1103/PhysRevX.9.031042> for details of curve fitting.
- [37] L. Nie, A. V. Maharaj, E. Fradkin, and S. A. Kivelson, *Vestigial Nematicity from Spin and/or Charge Order in the Cuprates*, *Phys. Rev. B* **96**, 085142 (2017).
- [38] T. Wu, H. Mayaffre, S. Krämer, M. Horvatić, C. Berthier, W. N. Hardy, R. Liang, D. A. Bonn, and M.-H. Julien, *Incipient Charge Order Observed by NMR in the Normal State of $\text{YBa}_2\text{Cu}_3\text{O}_y$* , *Nat. Commun.* **6**, 6438 (2015).
- [39] V. Thampy, S. Blanco-Canosa, M. Garcia-Fernandez, M. P. M. Dean, G. D. Gu, M. Först, T. Loew, B. Keimer, M. Le Tacon, S. B. Wilkins, and J. P. Hill, *Comparison of Charge Modulations in $\text{La}_{1.875}\text{Ba}_{0.125}\text{CuO}_4$ and $\text{YBa}_2\text{Cu}_3\text{O}_{6.6}$* , *Phys. Rev. B* **88**, 024505 (2013).
- [40] E. H. da Silva Neto, M. Minola, B. Yu, W. Tabis, M. Bluschke, D. Unruh, H. Suzuki, Y. Li, G. Yu, D. Betto, K. Kummer, F. Yakhov, N. B. Brookes, M. Le Tacon, M. Greven, B. Keimer, and A. Damascelli, *Coupling between Dynamic Magnetic and Charge-Order Correlations in the Cuprate Superconductor $\text{Nd}_{2-x}\text{Ce}_x\text{CuO}_4$* , *Phys. Rev. B* **98**, 161114(R) (2018).
- [41] T. Hanaguri, C. Lupien, Y. Kohsaka, D.-H. Lee, M. Azuma, M. Takano, H. Takagi, and J. C. Davis, *A “Checkerboard” Electronic Crystal State in Lightly Hole-Doped $\text{Ca}_{2-x}\text{Na}_x\text{CuO}_2\text{Cl}_2$* , *Nature (London)* **430**, 1001 (2004).
- [42] C. Howald, H. Eisaki, N. Kaneko, and A. Kapitulnik, *Coexistence of Periodic Modulation of Quasiparticle States and Superconductivity in $\text{Bi}_2\text{Sr}_2\text{CaCu}_2\text{O}_{8+\delta}$* , *Proc. Natl. Acad. Sci. U.S.A.* **100**, 9705 (2003).
- [43] A. Mesaros, K. Fujita, S. D. Edkins, M. H. Hamidian, H. Eisaki, S.-i. Uchida, J. C. S. Davis, M. J. Lawler, and E.-A. Kim, *Commensurate $4a_0$ -Period Charge Density Modulations throughout the $\text{Bi}_2\text{Sr}_2\text{CaCu}_2\text{O}_{8+x}$ Pseudogap Regime*, *Proc. Natl. Acad. Sci. U.S.A.* **113**, 12661 (2016).
- [44] J. Lorenzana and G. Seibold, *Metallic Mean-Field Stripes, Incommensurability, and Chemical Potential in Cuprates*, *Phys. Rev. Lett.* **89**, 136401 (2002).
- [45] B. Ponsioen, S. S. Chung, and P. Corboz, *Period 4 Stripe in the Extended Two-Dimensional Hubbard Model*, *arXiv:1907.01909*.
- [46] K. Ishizaka, T. Arima, Y. Murakami, R. Kajimoto, H. Yoshizawa, N. Nagaosa, and Y. Tokura, *Commensurate-Incommensurate Crossover of Charge Stripe in $\text{La}_{2-x}\text{Sr}_x\text{NiO}_4$ ($x \sim 1/3$)*, *Phys. Rev. Lett.* **92**, 196404 (2004).
- [47] S. B. Wilkins, M. P. M. Dean, J. Fink, M. Hücker, J. Geck, V. Soltwisch, E. Schierle, E. Weschke, G. Gu, S. Uchida, N. Ichikawa, J. M. Tranquada, and J. P. Hill, *Comparison of Stripe Modulations in $\text{La}_{1.875}\text{Ba}_{0.125}\text{CuO}_4$ and $\text{La}_{1.48}\text{Nd}_{0.4}\text{Sr}_{0.12}\text{CuO}_4$* , *Phys. Rev. B* **84**, 195101 (2011).
- [48] M. P. M. Dean, G. Dellea, R. S. Springell, F. Yakhov-Harris, K. Kummer, N. B. Brookes, X. Liu, Y.-J. Sun, J. Strle, T. Schmitt, L. Braicovich, G. Ghiringhelli, I. Bozovic, and J. P. Hill, *Persistence of Magnetic Excitations in $\text{La}_{2-x}\text{Sr}_x\text{CuO}_4$ from the Undoped Insulator to the Heavily Overdoped Non-superconducting Metal*, *Nat. Mater.* **12**, 1019 (2013).
- [49] G. Seibold and J. Lorenzana, *Stability of Metallic Stripes in the One-Band Extended Hubbard Model*, *Phys. Rev. B* **69**, 134513 (2004).
- [50] K. Yamada, C. H. Lee, K. Kurahashi, J. Wada, S. Wakimoto, S. Ueki, H. Kimura, Y. Endoh, S. Hosoya, G. Shirane, R. J. Birgeneau, M. Greven, M. A. Kastner, and Y. J. Kim, *Doping Dependence of the Spatially Modulated Dynamical Spin Correlations and the Superconducting-Transition Temperature in $\text{La}_{2-x}\text{Sr}_x\text{CuO}_4$* , *Phys. Rev. B* **57**, 6165 (1998).
- [51] P. A. Lee, T. M. Rice, and P. W. Anderson, *Conductivity from Charge or Spin Density Waves*, *Solid State Commun.* **14**, 703 (1974).
- [52] S. R. White and D. J. Scalapino, *Stripes on a 6-Leg Hubbard Ladder*, *Phys. Rev. Lett.* **91**, 136403 (2003).
- [53] M. Bosch, W. van Saarloos, and J. Zaanen, *Shifting Bragg Peaks of Cuprate Stripes as Possible Indications for Fractionally Charged Kinks*, *Phys. Rev. B* **63**, 092501 (2001).
- [54] V. I. Anisimov, M. A. Korotin, A. S. Mylnikova, A. V. Kozhevnikov, D. M. Korotin, and J. Lorenzana, *Computation of Stripes in Cuprates within the LDA + U Method*, *Phys. Rev. B* **70**, 172501 (2004).